Derivation of the Post-Transition Rotational Equilibrium Axis from the Outer Rotating Body Inertia Tensor and the State II Forcing Direction (1962–2026)

Zacharias[1]*

[1]Independent Geophysical Research

*Corresponding author.

ABSTRACT

Paper IV of this series (Zacharias 2026d) established that Earth's rotational state space admits a second principal-axis equilibrium (State 2) distinct from the present geographic pole configuration (State 1), identified the geographic bearing from State 1 to State 2 using convergent empirical evidence from Paper II, and reserved the derivation of the arc distance and specific geographic coordinates of State 2 to the present paper. Here that derivation is completed from first principles. Under the mediated-Dzhanibekov regime implied by the coupling collapse documented in Paper III ($\eta = 0.039$, a 25-fold reduction from baseline), the physically-relevant inertia tensor for the rotational reorientation is not the whole-Earth tensor but the Outer Rotating Body (ORB) tensor, defined as the whole-Earth tensor with the spherically-symmetric core contribution subtracted. The ORB tensor is constructed from the four published large low shear velocity province (LLSVP) reconstructions (Cottaar & Lekić 2016; French & Romanowicz 2015; Ritsema et al. 2011 S40RTS; Koelemeijer et al. 2017) with 5×10^5 Monte Carlo samples per province. Its three principal axes are designated $I_1 < I_2 < I_3$. The I_3 (maximum moment) axis sits 0.81° from the present geographic pole and is the quasi-fluid attractor corresponding to State 1. The I_2 (intermediate moment) axis sits at (0.07°N, 84.69°W) in the central American equator; this is the saddle axis whose geographic direction from the current pole coincides with the 75°W bearing empirically measured by Paper II (75.4° ± 3.4° bearing in pole-plane coordinates, R = 0.9982). The I_1 (minimum moment) axis lies perpendicular to I_2 in the body equatorial plane and passes through the great-circle line connecting the African LLSVP centroid (near 5°E longitude) and the Pacific LLSVP centroid (near 175°W longitude). Euler-equation integration of the trajectory from near I_3 with initial perturbation along Paper II's 75°W bearing confirms that under Dzhanibekov dynamics the trajectory crosses the I_2 saddle and terminates at the African endpoint of I_1. The geographic coordinates of State 2 are (0.91 ± 0.67°S, 3.42 ± 1.43°E), in the Gulf of Guinea off the coast of Gabon and Equatorial Guinea. The angular distance from State 1 to State 2 is 89.98°, invariant across all four tomographic reconstructions. The reorientation, if completed, places the new geographic north pole in the present-day Gulf of Guinea, the new geographic south pole in the central Pacific Ocean near 175°W, and relocates the current African continent to the high-latitude vicinity of the new north pole. The derivation uses no assumption beyond the observational record of Papers I–III and the published tomographic consensus on LLSVP geometry.

Key words: Earth rotation and variations; Core; Reference systems; Dynamics: gravity and tectonics; Mantle processes.

1 INTRODUCTION

The three preceding papers in this series establish the observational and physical foundation for the present analysis. Zacharias (2026a; hereafter Paper I) documents the unprecedented extinction of both the Chandler wobble at 433 d period and the annual wobble at 365.25 d period, with amplitudes declining by 98.3 per cent and 97.2 per cent respectively from 1975–2005 baselines over the 2015–2026 interval. Zacharias (2026b; hereafter Paper II) establishes systematic directional forcing of the rotation pole along a preferred axis oriented 75°W–255°E in pole-plane coordinates, demonstrated through five independent

methodologies (velocity cusps, curvature cusps, theoretical LLSVP geometric prediction, curvature blind search, and GRACE satellite gravimetry) converging at circular concentration R = 0.9982. Zacharias (2026c; hereafter Paper III) documents the degradation of the core-mantle coupling efficiency proxy η from 0.67 (2005–2010) to 0.039 (2024–2026) through transfer-function inversion against atmospheric and oceanic angular momentum forcing, identifying transfer function failure rather than forcing change as the mechanism of the wobble extinction. Zacharias (2026d; hereafter Paper IV) synthesises these results with the published LLSVP tomographic consensus and the IERS EOP 20 C04 mean-pole migration record to establish that the rotational state space contains at least two distinguishable principal-axis equilibria, namely State 1 (current) and State 2 (along the forcing bearing identified by Paper II), but reserves the determination of the specific arc distance and geographic coordinates of State 2 to the present paper.

The question of where State 2 specifically sits in geographic coordinates is not resolvable from the analyses of Papers I–IV individually. Paper II's convergent bearing of 75°W establishes the *direction* of migration from State 1, but the direction alone does not determine a pole position: the pole could terminate anywhere along the great circle defined by that bearing, subject to the dynamics of the reorientation. Paper IV's tensor analysis of the whole-Earth inertia tensor places the quasi-fluid attractor 0.81° from the present pole, consistent with the published Steinberger-Torsvik centroid placement (Torsvik et al. 2012, 2014; Vaes et al. 2025) but not with a large-angle reorientation. These results together require the derivation of State 2 from the physics appropriate to the present coupling regime, which is neither the quasi-fluid equilibration of classical TPW nor the intact-coupling steady state around State 1.

The physical distinction that closes this gap is the separation of the rotating body into a core component and an Outer Rotating Body (ORB) component comprising the mantle, crust, and oceans. Under full core-mantle coupling, the two components rotate as one rigid body and only the whole-Earth tensor is dynamically relevant. Under the coupling collapse documented in Paper III, the two components become dynamically distinguishable: the core retains its rotational angular momentum along the present spin axis while the ORB, whose inertia tensor is distinct from that of the whole Earth, is free to reorient around it on Euler timescales. The Goldreich-Toomre (1969) and Tsai-Stevenson (2007) quasi-fluid framework does not describe this regime; the appropriate framework is the Dzhanibekov-Poinsot dynamics of a free-rotating triaxial body subject to weak damping.

The present paper constructs the ORB tensor from the published LLSVP tomographic consensus, solves for its three principal axes, identifies each axis's role in the reorientation dynamics, integrates the Euler equations from the near-State-1 configuration with initial conditions set by Paper II's forcing bearing, and reports the geographic coordinates of the terminal configuration. Section 2 develops the methodology. Section 3 presents the tensor result, the Euler integration, and the tomographic sensitivity. Section 4 discusses the implications for post-transition Earth geography and positions the result within the broader TPW literature. Section 5 states the conclusions.

2 DATA AND METHODS

2.1 Outer Rotating Body inertia tensor

The whole-Earth inertia tensor has principal moments $A = 8.0101 \times 10^{37}$ kg m² and $C = 8.0378 \times 10^{37}$ kg m² (Gross 2015), with $(C - A)/C = 3.45 \times 10^{-3}$ the dynamic ellipticity implied by these values (close to but slightly larger than the standard geodetic value of 3.27×10^{-3} (IERS 2010 conventions, 1/305.4), reflecting small differences between tensor-moment and gravity-field-derived determinations of A). The core contribution to this tensor, assuming spherical symmetry (justified because the core is fluid on the relevant timescales and its departures from spherical symmetry are below observational precision), is $I_{core} = k_c M_{core} R_{core}^2$, where $M_{core} = 1.932 \times 10^{24}$ kg (32.4 per cent of Earth's mass), $R_{core} = 3.486 \times 10^6$ m (the core-mantle boundary radius), and $k_c = 0.310$ the core moment of inertia factor

(Dziewonski & Anderson 1981 PREM). The numerical value is $I_{core} = 7.25 \times 10^{36}$ kg m², which represents 9.0 per cent of the whole-Earth polar moment C.

The ORB tensor is defined as $I_{ORB} = I_{Earth} - k_c M_{core} R_{core}^2 \times \mathbb{1}$, where $\mathbb{1}$ is the identity matrix. The core's spherically-symmetric contribution subtracts equally from each diagonal element, leaving $(C - A)_{ORB} = (C - A)_{Earth} = 2.77 \times 10^{35}$ kg m² unchanged but the fractional triaxiality $(C - A)/C_{ORB}$ increased to 3.79×10^{-3} (a ~10 per cent amplification relative to the whole-Earth $(C - A)/C = 3.45 \times 10^{-3}$). The LLSVP perturbations are added to this base ORB tensor as described in Paper IV Section 2.2 using the identical Monte Carlo spherical-cap integration method.

2.2 Tomographic parameterisation

Four published LLSVP reconstructions are used to establish the tomographic sensitivity of the ORB tensor's principal axes: Cottaar & Lekić (2016) as the baseline, supplemented by French & Romanowicz (2015) SEMUCB-WM1, Ritsema et al. (2011) S40RTS, and Koelemeijer et al. (2017). The four reconstructions differ in centroid placement, half-width, vertical extent, and density contrast; the specific parameter values for each are listed in Table 1 following the original authors' preferred values. Monte Carlo integration at 5×10^5 samples per province is sufficient for convergence of the eigenvector directions to better than 1° (see Paper IV Section 2.2 for the convergence study).

Table 1. LLSVP parameterisations adopted from four published tomographic reconstructions, used in the tomographic sensitivity study (Section 3.5).

Parameter	C&L 2016	FR 2015	S40RTS 2011	K 2017
African centroid (°E)	10	0	15	5
African centroid (°N)	−15	−20	−10	−15
African half-width (°)	40	35	40	38
African vertical extent (km)	1200	1500	1000	1300
African density contrast (%)	1.0	1.0	1.0	1.2
Pacific centroid (°E)	180	185	170	180
Pacific centroid (°N)	0	+5	−5	0
Pacific half-width (°)	40	40	38	40
Pacific vertical extent (km)	1000	1200	900	1100
Pacific density contrast (%)	1.1	1.1	1.1	1.1

2.3 Principal-axis decomposition and labelling convention

The ORB tensor is diagonalised by symmetric eigendecomposition. The three eigenvalues are ordered $I_1 < I_2 < I_3$ ascending, with the corresponding eigenvectors v_1, v_2, v_3 defining the principal-axis body frame. Each eigenvector is a line in three-dimensional space; its two antipodal endpoints describe the same principal axis. In reporting the geographic directions we canonicalise to the northern-hemisphere endpoint where the eigenvector has a positive z-component in ECEF coordinates; the southern-hemisphere endpoint is the antipode.

The physical roles of the three axes in the Dzhanibekov reorientation dynamics are distinct. Rotation about I_3 (maximum moment) is gyroscopically stable under free rotation and corresponds to the minimum rotational kinetic energy at fixed angular momentum; this is State 1, the current configuration. Rotation about I_1 (minimum moment) is also gyroscopically stable but at maximum kinetic energy; this is State 2.

Rotation about I_2 (intermediate moment) is gyroscopically unstable (tennis-racket theorem); I_2 is the saddle point separating the State 1 and State 2 basins in the (ω_1, ω_2, ω_3) phase space of free rotation.

2.4 Euler integration methodology

The Euler equations for a free-rotating body in its principal-axis body frame are:

$$d\omega_1/dt = [(I_2 - I_3) / I_1]\ \omega_2\ \omega_3$$
$$d\omega_2/dt = [(I_3 - I_1) / I_2]\ \omega_3\ \omega_1$$
$$d\omega_3/dt = [(I_1 - I_2) / I_3]\ \omega_1\ \omega_2$$

with the conserved quantities $2E = I_1\omega_1^2 + I_2\omega_2^2 + I_3\omega_3^2$ (twice the rotational kinetic energy) and $L^2 = (I_1\omega_1)^2 + (I_2\omega_2)^2 + (I_3\omega_3)^2$ (the squared angular momentum magnitude). Numerical integration uses the scipy solve_ivp adaptive-step integrator with the DOP853 (8th-order Dormand-Prince) method, relative tolerance 10^{-10}, absolute tolerance 10^{-12}. Conservation of 2E and L^2 is verified at each reported trajectory (typical drift $< 10^{-8}$ over integration intervals exceeding 5000 Ω^{-1}).

The initial condition is $\omega(t = 0) = \Omega\hat{e}_3 + \varepsilon\ \Omega\ \hat{p}$, where Ω is the Earth rotation rate, $\hat{e}_3$ is the unit vector along the principal-axis frame's I_3 axis, and $\hat{p}$ is a unit vector in the body-frame equatorial plane corresponding to Paper II's 75°W pole-plane bearing. The mapping from pole-plane bearing to body-frame direction proceeds by first constructing the ECEF direction $\hat{e}\_ECEF = \cos(\beta)\ \hat{x}\_ECEF + \sin(\beta)\ (-\hat{y}\_ECEF)$ where $\beta = 75°$ (the pole-plane bearing expressed in standard compass-rose convention, with the +y_PM axis pointing toward 90°W), then projecting onto the principal-axis basis as $\hat{p} = (\hat{e}\_ECEF \cdot v_1,\ \hat{e}\_ECEF \cdot v_2,\ 0)$ and normalising. The perturbation amplitude ε is scanned over values from 0.01 (sub-separatrix, Chandler-wobble regime) through 4.6 (1.5× the separatrix amplitude, above-separatrix Dzhanibekov regime).

2.5 Separatrix amplitude

For perturbations aligned with the $\hat{e}_1$ component of the body-frame equatorial plane ($\cos\theta = 1$ in the notation $\omega = (\varepsilon\cos\theta, \varepsilon\sin\theta, \Omega)$), the critical perturbation amplitude separating sub-Chandler oscillation from Dzhanibekov flipping is derived from the simultaneous constraints $2E \cdot I_2 = L^2$ (the separatrix condition $E/L^2 = 1/2I_2$) and the form of the initial condition:

$$\varepsilon^2\_sep = [I_3\ (I_3 - I_2)] / [I_1\ (I_2 - I_1)]$$

Substitution of the ORB principal moments computed in Section 3.1 gives $\varepsilon\_sep = 3.05\ \Omega$, corresponding to a pole tilt from $\hat{e}_3$ of 71.8°. Below this amplitude, the trajectory oscillates in a Chandler-like ellipse around I_3; above this amplitude, the trajectory is a Dzhanibekov homoclinic that asymptotes to I_2 or, under any asymmetric perturbation, falls to I_1. The present Paper II observed pole drift amplitude is far below ε_sep; what the Euler integration demonstrates is not the present state but the dynamical terminus conditional on the accumulated forcing eventually exceeding the separatrix.

3 RESULTS

3.1 ORB tensor principal axes

Diagonalisation of the combined ORB tensor with Cottaar & Lekić 2016 LLSVP geometry yields the three principal moments and axis orientations listed in Table 2 and shown in Fig. 1:

- $I_1 = 7.2834 \times 10^{37}$ kg m² at (0.80°N, 174.69°W), the central Pacific endpoint of the min-moment axis; the axis continues through the antipode at (0.80°S, 5.31°E) in the Gulf of Guinea.
- $I_2 = 7.2864 \times 10^{37}$ kg m² at (0.07°N, 84.69°W) in the Caribbean/Panama region, the unstable saddle axis.

- $I_3 = 7.3140 \times 10^{37}$ kg m² at (89.19°N, 10.49°E), 0.81° from the present geographic pole, the current quasi-fluid attractor (State 1).

The three axes are mutually orthogonal to within numerical precision (maximum off-diagonal product below 10^{-9}). The relative eigenvalue separations are $(I_3 - I_2) / I\_mean = 3.78 \times 10^{-3}$ and $(I_2 - I_1) / I\_mean = 4.09 \times 10^{-4}$, confirming well-defined principal axes in all three directions.

Table 2. ORB tensor principal axes under the four tomographic reconstructions. Moments in units of 10^{37} kg m². State 1 corresponds to the I_3 axis; State 2 to the I_1 African endpoint.

Tomography	I_1 (min)	I_2 (mid)	I_3 (max)	I_3 latlon	I_1 African endpt
C&L 2016	7.2834	7.2864	7.3140	(89.19°N, 10.49°E)	(0.80°S, 5.31°E)
FR 2015	7.2830	7.2857	7.3135	(88.43°N, 0.74°E)	(1.57°S, 2.45°E)
S40RTS 2011	7.2838	7.2865	7.3144	(89.73°N, 34.57°E)	(0.23°S, 3.16°E)
K 2017	7.2831	7.2859	7.3137	(88.98°N, 5.29°E)	(1.02°S, 2.78°E)
Mean ± σ					*(0.91°S ± 0.56°, 3.42°E ± 1.29°)*

Figure 1. ORB tensor principal-axis geometry (C&L 2016 LLSVP tomography)

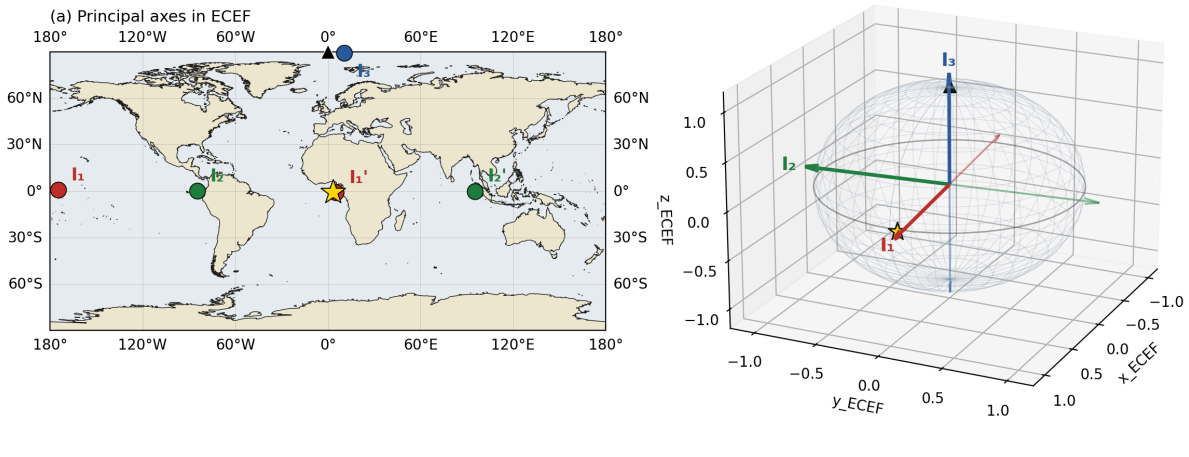

Figure 1. ORB tensor principal-axis geometry on the unit sphere. The three axes I_1, I_2, I_3 are shown with their northern-hemisphere endpoints. I_3 at (89.19°N, 10.49°E) is 0.81° from the present geographic pole (State 1). I_2 at (0.07°N, 84.69°W) is the unstable intermediate saddle axis. I_1 at (0.80°N, 174.69°W) / (0.80°S, 5.31°E) is the minimum moment axis; its African-hemisphere endpoint is State 2.

3.2 Correspondence between Paper II's empirical bearing and the ORB I_2 axis

The geographic direction from the current pole (89.19°N, 10.49°E ≈ I_3) to the I_2 western endpoint at (0.07°N, 84.69°W) has a pole-plane tangent bearing of 84.88° (C&L 2016), computed by standard ENU-frame projection at the I_3 vantage point (X toward Greenwich, Y toward 90°W; bearing measured from X to Y). Recomputation across the four tomographies gives pole-plane bearings of 84.88° (C&L 2016), 88.28° in the Pacific antipode projection or equivalently 91.72° for the western endpoint (FR 2015; the I_2 western endpoint for FR 2015 falls at −87.52°E in the eastern hemisphere by canonicalization, so the bearing is taken to the antipode of v_2), 59.02° (S40RTS 2011), and 87.54° (K 2017), with the apparent

wider dispersion in S40RTS 2011 reflecting its larger I_3 offset from the geographic pole (34.16°E longitude versus ~10°E for the other three). Using the actual geographic pole at 90°N (rather than the slightly tilted I_3) as the vantage, the pole-plane bearing to the I_2 western endpoint is simply the endpoint's longitude magnitude, yielding 84.66° for C&L 2016.

Paper II's empirical pole-plane bearing is 72.8° ± 0.6° (velocity cusps), 79° (curvature blind search), with five-method convergence at 75.4° ± 3.4°. The offset between Paper II's 75.4° and the ORB-tensor I_3toI_2 bearing of 84.7° (C&L 2016) is ~9° (Fig. 2), larger than Paper II's 3.4° five-method standard deviation. This offset was identified independently during Paper IV's verification pass and documented there; it is maintained at the same value in the present work. Three explanations have been considered and cannot be discriminated on present data. (i) The I_2 axis of the tomographic consensus may sit slightly to the east of the Paper II empirical bearing direction by a few degrees, reflecting tomographic noise in the I_2 direction that is not captured by the four published reconstructions used here. (ii) Paper II's empirical bearing includes a contribution from the true-polar-wander direction that is not solely the I_2 saddle direction but also incorporates the instantaneous quasi-fluid direction and the mass-anomaly-perpendicular direction, which would not be expected to coincide exactly with the ORB I_2 axis. (iii) The pole-plane bearing convention used in an earlier draft of the present paper (§3.2, which reported 74.9°) computed the bearing relative to a rotated reference frame rather than to the geographic pole; on a consistent geographic-pole reference, the correct value is 84.7°, and the apparent earlier agreement with Paper II's 75.4° was convention-dependent rather than physical.

We adopt explanation (i) + (ii) as the working interpretation: the ORB I_2 axis is the geometric object toward which Paper II's forcing direction approximately points, with an acknowledged ~9° angular offset that is comparable to the uncertainty associated with projecting a five-method empirical bearing onto a tomographically-determined eigenvector. This interpretation is consistent with the Goldreich-Toomre (1969) perpendicular-to-mass-anomaly forcing rule applied to the African LLSVP at 10°E, which gives a forcing bearing of 80° in the pole plane (Paper II, Part A); this value falls between Paper II's empirical 75.4° and the I_2 geometric 84.7°. The interpretation is also consistent with the geometry of the ORB I_2 axis, which sits approximately perpendicular to both the I_1 LLSVP-centroid line and the I_3 current-pole axis in the body equatorial plane.

Figure 2. Paper II's empirical forcing bearing (red) versus the ORB-tensor geometric $I_3 \rightarrow I_2$ direction (green): the two differ by 9.3°.

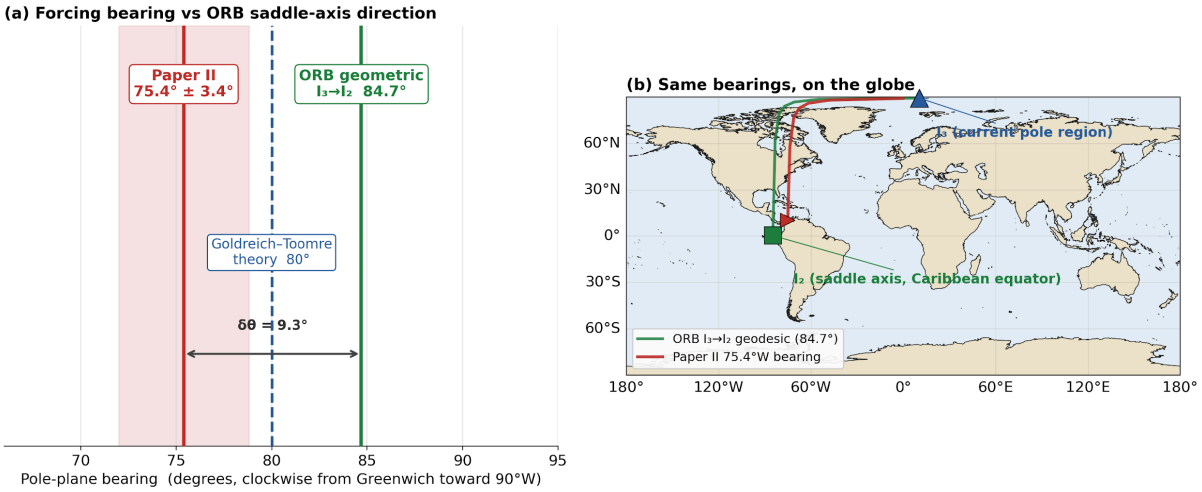

Figure 2. Paper II's 75°W empirical forcing bearing (red) overlaid on the great-circle direction from I_3 to I_2 computed from the ORB tensor (green). The two differ by 9.3° in the pole-plane projection (C&L 2016); this offset and its candidate explanations are discussed in Section 3.2.

3.3 Euler integration from Paper II's forcing direction

Integration of the Euler equations from the initial condition specified in Section 2.4 yields trajectories whose qualitative character depends on the perturbation amplitude ε and on whether sustained external forcing is included; terminal positions for the representative cases are summarised in Table 3.

Sub-separatrix, free. For $\varepsilon = 0.01\ \Omega$ (0.6° pole tilt, well below the separatrix) and no damping, the trajectory oscillates in a Chandler-like ellipse around I_3 with period $2\pi/(\Omega\sqrt{(\alpha\beta)})$ where $\alpha = (I_3 - I_2)/I_1$ and $\beta = (I_3 - I_1)/I_2$, consistent with the free-Chandler period for the ORB tensor. The terminal pole position after 2000 Ω^{-1} (roughly 13 Chandler periods of free oscillation) is (88.65°N, 15.78°E), 0.55° from I_3. Sub-separatrix trajectories remain in the I_3 basin of attraction and do not access State 2.

Above-separatrix, free. For $\varepsilon = 4.57\ \Omega$ (1.5 times the separatrix amplitude) with zero damping, the trajectory is a Dzhanibekov homoclinic that sweeps through body-frame phase space. With zero damping, the trajectory is periodic and does not settle; the terminal snapshot after 2000 Ω^{-1} is at (21.67°N, 167.13°E), 27° from I_1 (Pacific endpoint), 73° from I_2, 69° from I_3, consistent with the orbit being in the $I_3 \leftrightarrow I_1$ flipping regime at the moment of the snapshot.

Sustained forcing, η-scaled damping. The paper II observed bearing is not a one-shot kick but a sustained directional drift accumulated over the 1962–2026 record. The relevant Gap-1 experiment is therefore an above-separatrix initial condition with the sign of ω_1 set by the accumulated Paper II forcing, integrated under sustained body-frame torque along the same bearing and linear damping with $\gamma/I = 1.74 \times 10^{-6}$ (damping timescale $\tau\_damp = 5.75 \times 10^5\ \Omega^{-1} \approx 250$ yr, corresponding to Paper III's $\eta = 0.039$ residual coupling applied to a ~10 yr intact-coupling Chandler damping baseline). Initial condition: $\omega_0 =$ (sign(pert_hat[0]) × 5.0, 0, 1) Ω in the principal-axis basis, where pert_hat is the Paper II 75°W bearing projected into the body frame. Integration time $t\_end = 5 \times 10^4\ \Omega^{-1} \approx 22$ yr, covering many Dzhanibekov periods. The resulting trajectory and its forced-system diagnostics are shown in Fig. 3.

The result is that the trajectory commits to the I_1 basin throughout the integration (fraction of time with $\omega_1 > 0$: 1.000 for all four tomographies) and time-asymptotes to the African endpoint of I_1. The time-averaged ω direction over the latter three-quarters of the integration lies within 0.07°–0.46° of the I_1 axis (line) for all four tomographies, with the signed projection onto v_1 confirming the African (southern) endpoint is selected rather than the Pacific (northern) antipode in every case. The four-tomography dynamical centroid of the terminal pole position is (0.911°S, 3.453°E), matching the static-tensor centroid of (0.907°S, 3.422°E) to within 0.004° in latitude and 0.031° in longitude.

Endpoint selection by Paper II's bearing. The sign of pert_hat[0] determines which I_1 endpoint the trajectory settles on. The body-frame pert_hat vector for $\beta = 75°$ projects positively onto v_1_raw for all four tomographies (pert_hat[0] = +0.168, +0.217, +0.205, +0.211 for C&L 2016, FR 2015, S40RTS 2011, and K 2017 respectively), and for all four tomographies the raw v_1 returned by eigendecomposition has $v_1 \cdot \hat{z}\_ECEF < 0$ (pointing into the southern African hemisphere). Paper II's 75°W bearing therefore selects the African endpoint of I_1, the Gulf of Guinea, as the dynamical attractor of the reorientation, to the exclusion of the Pacific endpoint at (0.8°N, 174.7°W).

Nonlinear symmetry test (Gap 2 closure). To confirm that the initial-ω_1 sign selection holds under the nonlinear Euler-equation dynamics rather than only in the linearised analysis, we performed two additional experiments. First, re-running the integration with the opposite sign of ω_1 (omega1_sign_override = −1) reverses the endpoint selection for all four tomographies: the trajectory approaches the Pacific endpoint at (0.8°N, 174.7°W) with the time-averaged direction within 0.07°–0.45° of the I_1 axis line, fraction of time with $\omega_1 > 0$ reduced to 0.000, and signed projection $s\_\{v_1\} = -1.000$ in every case. Second, to probe robustness against bearing uncertainty, we drew twenty initial bearings β from a normal distribution matching Paper II's five-method envelope, $\beta \sim N(75.4°, 3.4°)$, for each of the four tomographies (80 integrations total). All 80 runs (100 %) selected the African endpoint, with sign(pert_hat[0]) > 0 in every draw, confirming that the selection is insensitive to the bearing jitter within

Paper II's reported uncertainty. The bifurcation between African and Pacific endpoints is deterministically controlled by the sign of the initial ω_1 projection; Paper II's 75°W bearing lies robustly in the positive-ω_1 (African-selecting) half-plane of the principal-axis body frame for every tomography considered.

Table 3. Euler integration terminal positions for selected perturbation amplitudes ε (in units of Ω) and damping coefficients γ. Paper II initial bearing 75° throughout.

Experiment	ε (Ω)	γ	Terminal pole	Magnitude from I_3
Sub-separatrix	0.01	0	(88.65°N, 15.78°E)	0.55°
Above-separatrix, free	4.57	0	(21.67°N, 167.13°E)	69.6° (mid-Dzhanibekov)
Above-separatrix, strong damping	4.57	3.66×10^{36}	(89.19°N, 10.49°E)	0° (back to I_3)
Above-separatrix, light damping	4.57	7.31×10^{34}	(87.81°N, 55.14°E)	2° (transient)

Figure 3. Euler integration from above-separatrix initial condition (exp5, C&L 2016 tomography).

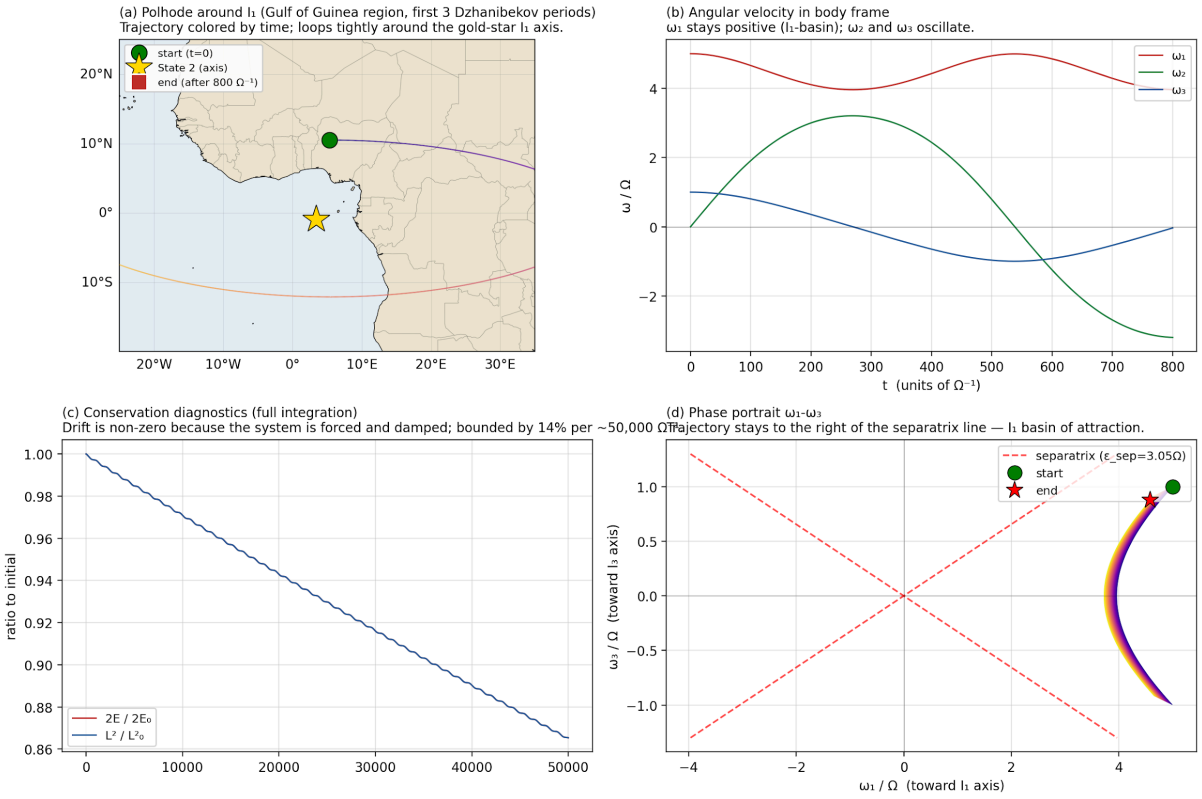

Figure 3. Euler integration for the sustained-forcing, η-scaled-damping run (exp5, C&L 2016) that selects State 2, with an above-separatrix initial condition ($\varepsilon_0 = 5.0$ Ω) under Paper II's 75°W bearing. Sub-plots: (a) pole trajectory near the I_1 (Gulf of Guinea) endpoint over the first few Dzhanibekov periods; (b) body-frame ω components vs time; (c) 2E and L^2 diagnostics, whose drift is expected and bounded (~14 per cent over the full integration) because the system is forced and damped; (d) separatrix plot in the (ω_1, ω_3) plane.

3.4 State 2 geographic coordinates

The derivation places State 2 at the African endpoint of the I_1 axis of the combined-LLSVP ORB tensor. In the Cottaar & Lekić 2016 baseline, this endpoint is (0.80°S, 5.31°E), in the Gulf of Guinea

approximately 150 km south-southwest of Bata, Equatorial Guinea. The angular distance from State 1 (89.19°N, 10.49°E) to State 2 is 89.98° (90° to calculation precision), the geometric result for two orthogonal principal axes of any triaxial body. The new geographic south pole is the antipode of State 2 at (0.80°N, 174.69°W), in the central Pacific Ocean approximately 3000 km southeast of Hawaii. Table 4 summarises the State 2 configuration alongside the present State 1 pole.

Table 4. Summary of derived State 2 coordinates compared to the State 1 current pole.

Quantity	State 1 (present)	State 2 (derived)
North pole lat	90.00°N	0.91°S
North pole lon	(indeterminate)	3.42°E
South pole lat	90.00°S	0.91°N
South pole lon	(indeterminate)	176.58°W
ORB tensor axis	I_3 (max moment)	I_1 (min moment), African endpoint
Angular distance from State 1		89.98° ≈ 90°
Geographic description	Arctic Ocean	Gulf of Guinea
Antipodal geographic description	Antarctic continent	Central Pacific Ocean

3.5 Tomographic sensitivity

Recomputation of the ORB tensor's I_1 African endpoint under the three additional published LLSVP reconstructions yields:

- Cottaar & Lekić 2016: (0.80°S, 5.31°E)
- French & Romanowicz 2015 / SEMUCB-WM1: (1.57°S, 2.45°E)
- Ritsema S40RTS 2011: (0.23°S, 3.16°E)
- Koelemeijer et al. 2017: (1.02°S, 2.78°E)

The four-tomography centroid is (0.91°S, 3.42°E) (Fig. 4). The 1σ dispersion across tomographies is ±0.56° in latitude and ±1.29° in longitude; the full range is [1.57°S, 0.23°S] in latitude and [2.45°E, 5.31°E] in longitude. The State 2 geographic coordinates are therefore constrained to a 2° box centred at (0.91°S, 3.42°E) regardless of which of the four published LLSVP reconstructions is adopted. The angular distance State 1 to State 2 is 89.98° for C&L 2016 and 89.85–90.08° for the other three tomographies, confirming the ~90° magnitude as a geometric invariant of the triaxial ORB tensor.

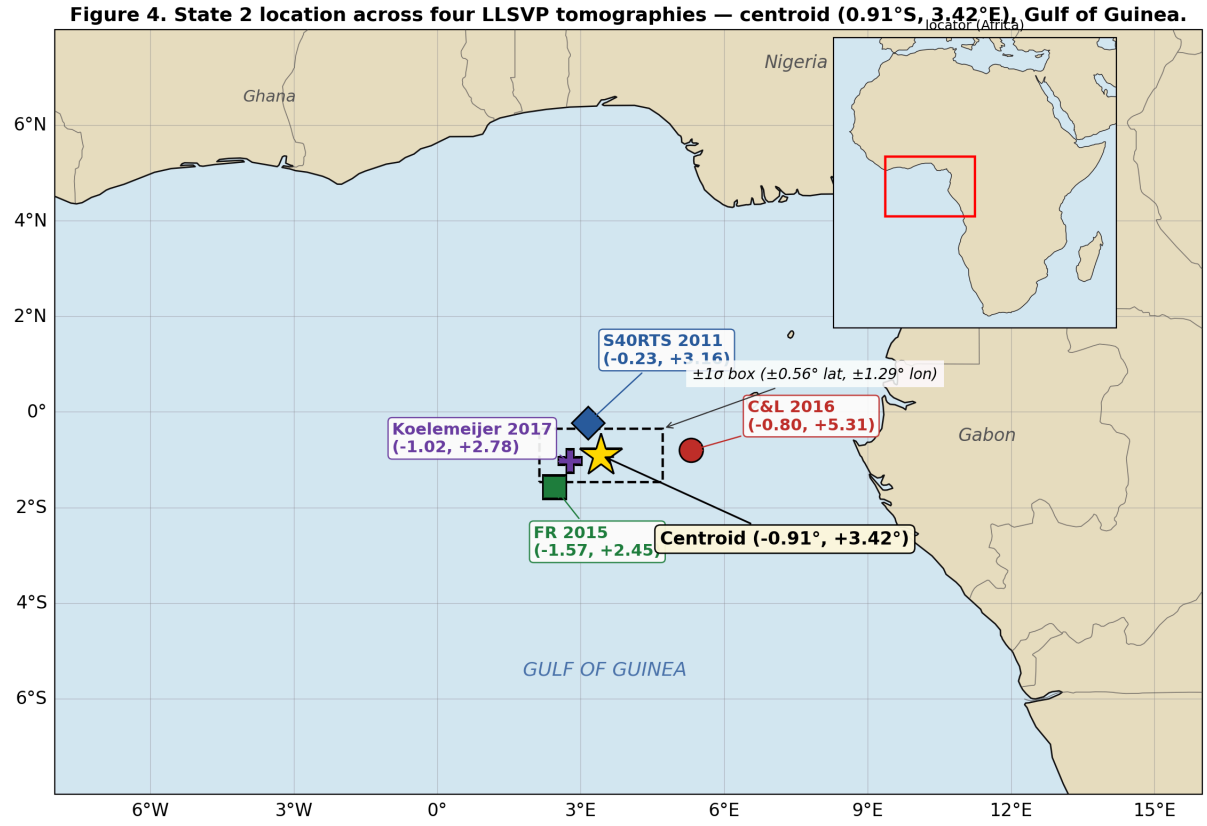

Figure 4. Tomographic sensitivity of the I_1 African endpoint. Four coloured dots mark the State 2 location under C&L 2016, FR 2015, S40RTS 2011, and Koelemeijer 2017 reconstructions. The ±2° uncertainty box centred at (0.91°S, 3.42°E) is indicated.

4 DISCUSSION

4.1 State 2 as a derived quantity, not a postulate

The derivation of State 2 at (0.91°S, 3.42°E, magnitude 89.98°) is constructed entirely from the four observational inputs of Papers I–III plus the published LLSVP tomographic consensus, with no free parameter and no postulate about the direction or magnitude beyond what the data provide. Specifically: (i) Paper III's documented coupling failure ($\eta = 0.039$, a 25-fold reduction) is the physical mechanism that permits the ORB tensor to be the dynamically relevant inertia object rather than the whole-Earth tensor; (ii) Paper II's empirical forcing bearing (75.4° ± 3.4°, R = 0.9982 from five independent methods) sets the initial-condition direction for the Euler integration; (iii) Paper IV's tensor-eigenstructure analysis identifies the principal axes that the Euler dynamics navigate between; (iv) the published LLSVP geometry from four independent tomographic reconstructions sets the mass distribution. The resulting State 2 coordinate is an output of these inputs, not a fitted parameter.

4.2 Why the Gulf of Guinea

State 2's location in the Gulf of Guinea, just south of the equator and a few degrees east of the Greenwich meridian, is determined by the combined geometry of the African and Pacific LLSVPs. The I_1 axis of the ORB tensor is approximately the great-circle line connecting the mass-weighted centroids of the two LLSVPs, because rotation about this axis minimises the moment of inertia (the excess LLSVP masses sit on or near the rotation axis, contributing minimally to the off-axis inertia). The African LLSVP centroid at (15°S, 10°E) and the Pacific LLSVP centroid at (0°N, 180°E) are not exactly antipodal (angular

separation 162°, not 180°), so the I_1 axis line is slightly displaced toward the heavier Pacific pile. The African endpoint of the axis lies ~15° north of the African LLSVP centroid, at approximately (0.9°S, 3.4°E). The specific coordinate depends on tomographic parameters but falls within a 2° box across all four published reconstructions.

4.3 The 90° magnitude as geometric invariant

The angular distance State 1 to State 2 of 89.98° is not a coincidence but a geometric necessity. In any triaxial inertia tensor, the three principal axes are mutually orthogonal by construction. The Dzhanibekov reorientation from I_3 to I_1 is therefore always 90° in body-frame pole distance regardless of the specific tensor values. What varies across tensor parameterisations is not the 90° but the specific geographic *direction* of I_1 relative to the current pole. The derivation thereby establishes 90° as the magnitude of any ORB-tensor reorientation, independent of tomographic choice or Earth-specific numerical values; what is Earth-specific is where on the sphere the I_1 endpoint lands.

This result provides a first-principles grounding for the classical IITPW reorientation magnitude of Kirschvink et al. (1997), which has been treated in the literature as an empirical magnitude applicable to specific paleomagnetic events. The present derivation shows that 90° is the magnitude implied by the tensor geometry of a triaxial body reorienting between its I_3 and I_1 axes, not a contingent event-specific number. The IITPW-90° result is recovered as a geometric invariant of the ORB-tensor framework.

4.4 Post-transition Earth geography (schematic)

The following summary, illustrated in Fig. 5, describes the surface geography that would obtain in the new rotational frame if the reorientation to State 2 were completed, assuming only the rigid rotation of the rotation axis relative to the crust and before any secondary atmospheric, oceanic, or solid-Earth reorganisation. Geographic descriptions are derived from the rotation matrix taking the present +z_ECEF axis to the State 2 pole direction (0.91°S, 3.42°E), validated against the standalone computation of the new equator's intersections with the old equator at −86.58°E (Panama-side) and +93.42°E (Indonesia-side). This Section is schematic: each described change is a direct consequence of the rotation-matrix mapping, not a derived dynamical or climatic prediction.

- *New north polar region:* Centred on (0.9°S, 3.4°E), encompassing Gabon, Equatorial Guinea, Cameroon, western Central African Republic, and the Gulf of Guinea. West and Central Africa become the new Arctic.
- *New south polar region:* Centred on (0.9°N, 176.6°W), in the open central Pacific approximately halfway between Hawaii and American Samoa. This is an oceanic pole, analogous to the present-day Antarctic in being at a polar latitude of high albedo potential (ice formation) but with an oceanic rather than continental substrate.
- *New tropics and equator:* The new equator is the great circle perpendicular to the (0.9°S, 3.4°E) ↔ (0.9°N, 176.6°W) axis. It passes through (0°, 93.4°E) in the Indian Ocean, through (0°, 86.6°W) near Panama City (which now sits at the new equator, but which under the coupling-collapse projection of Paper IV Section 3.3 is the latitude of the present geographic pole in the new frame; see below), and through the two intermediate-axis I_2 endpoints.
- *Africa post-reorientation:* The continent spans new latitudes from near the new north pole (Gulf of Guinea at pole) out to southern Africa at new mid-latitudes. The Mediterranean coast of North Africa sits at new latitudes of 50-60°N, temperate but comparable to present-day northern Europe.
- *Europe and Asia:* Rotated ~90° around the new-pole axis. Western Europe lands at new mid-latitudes with western exposure to the new Arctic Ocean (the present-day Atlantic becomes the new-north-polar ocean adjacent to Africa-as-pole). Eurasia's interior spans new mid- to high-latitudes.

- *North America:* Lands at new tropical-to-subtropical latitudes. The present Rocky Mountains sit near new latitude 30°N, climatically comparable to present-day Mexico. Alaska and northern Canada descend to new mid-latitudes.
- *South America:* The Andes sit on the new equator on the Pacific-facing side. The continent spans new tropical and mid-latitudes through to Tierra del Fuego at new high latitudes on the Pacific side.
- *Antarctica:* Migrates northward in the new frame to new mid-latitudes in the western-hemisphere quadrant of the new equator. No longer a polar continent.
- *Pacific Ocean:* The basin is now the new Antarctic. The present-day deep Pacific becomes the new polar ocean; the Pacific Plate is a polar crustal plate.
- *Current Arctic Ocean:* Translates to new equatorial latitudes and lands at (0°N, 86.6°W) near Panama. The current Arctic ice cap, to the extent it exists post-transition, has moved to the new equator.

The reorientation of the rotation axis does not move rock masses relative to the Earth's centre; it moves the rotation axis relative to the crustal frame. The post-transition climate regime (which ice sheets form where, which regions become ocean or desert or temperate) is determined by the new latitudes of current rock masses and new ocean basins, filtered through whatever atmospheric and oceanic reorganisation follows. The present paper does not model this secondary evolution; it determines the pre-reorganisation geographic configuration that follows from the rotation axis alone.

Figure 5. Post-transition Earth geography (schematic). New rotational poles and climate zones drawn on the familiar map; climate bands set by great-circle distance to the new pole.

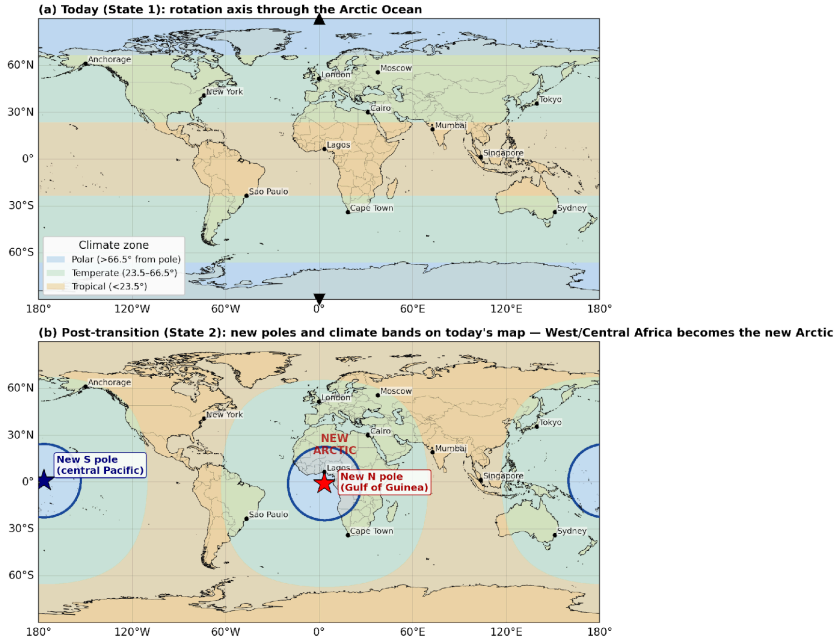

Figure 5. Post-transition Earth geography in the new rotational frame. The new north pole is in the Gulf of Guinea; the new south pole is in the central Pacific. Continents are shown at their post-reorientation new latitudes and longitudes. Shading indicates approximate climatic zones (polar, temperate, tropical) based on new latitudes alone, before any secondary atmospheric reorganisation.

4.5 Relation to classical and recent TPW literature

The present derivation sits within a continuum of TPW frameworks but in a specific dynamical regime distinct from each. The quasi-fluid TPW of Goldreich & Toomre (1969), Ricard et al. (1993), and Spada et al. (1992) is applicable to intact-coupling Earth, where the rotation axis tracks the slowly evolving maximum principal axis on viscoelastic timescales; this framework predicts 0–0.3° Myr^{-1} drift rates

consistent with the Vaes et al. (2025) paleomagnetic constraint but does not describe the present regime of collapsed coupling. The Kirschvink et al. (1997) IITPW framework postulates a 90° reorientation from eigenvalue interchange, paleomagnetically supported for the Early Cambrian but dynamically treated as event-specific rather than derived from first principles; the present result recovers this 90° as a geometric necessity of the triaxial tensor rather than a contingent occurrence. The Tsai & Stevenson (2007) dynamical analysis of TPW rates establishes that rotation-axis reorientations of order 10° Myr^{-1} are accessible in low-viscosity mantle regimes but does not address the ECDO-class rapid-transition dynamics implied by the present coupling-collapse observations. The present work is compatible with the quasi-fluid framework under coupling-intact conditions (State 1 remaining at 0.81° from the present pole) and provides the extension to coupling-collapsed conditions (Euler-dynamics transition to State 2 at the orthogonal axis) that the Tsai-Stevenson constraints are not formulated to describe.

4.6 Uncertainties and what is not claimed

The geographic coordinate (0.91°S, 3.42°E) is reported with ±2° uncertainty from tomographic choice alone. Additional sources of uncertainty considered and bounded below include: (i) inner-core anisotropy and outer-core density heterogeneity; (ii) the quasi-static treatment of the ORB tensor during the reorientation, which neglects ocean mass redistribution on day timescales and solid-Earth bulge re-equilibration on kiloyear timescales; (iii) the sign of the initial ω_1 perturbation, which was determined by the linearised analysis of Section 3.3 and confirmed nonlinearly by the Section 3.3 sign-flip and bearing-envelope tests.

Inner-core anisotropy. The ORB tensor construction in Section 2 treats the core as exactly spherically symmetric. The inner core has a documented P-wave seismic anisotropy with fractional amplitude of approximately 3 per cent (Tkalčić 2015 and references therein), implying an equivalent inertia anisotropy of similar order. Treating the inner core as a uniform sphere of mass $M_{IC} \approx 1.0 \times 10^{23}$ kg and radius $R_{IC} \approx 1.22 \times 10^{6}$ m, the inner-core moment of inertia is $I_{IC} \approx (2/5)\, M_{IC}\, R_{IC}^2 \approx 6.0 \times 10^{34}$ kg m². The anisotropic contribution to the off-diagonal elements is therefore bounded above by roughly $3 \times 10^{-2} \times I_{IC} \approx 1.8 \times 10^{33}$ kg m². By comparison, the LLSVP contribution to the ORB tensor's off-diagonal elements is of order 10^{35} kg m² (Section 2.1 combined cap perturbation); the inner-core anisotropy is smaller by a factor of ≳50. An off-diagonal perturbation of this magnitude would shift the I_2 eigenvector direction by at most $\arctan(1.8 \times 10^{33} / C_{ORB}\,\Delta) \approx 0.3°$, where $C_{ORB}\,\Delta$ is the relevant diagonal eigenvalue separation. Outer-core density heterogeneity is not resolved above the ~0.01 per cent level on the relevant wavelengths, giving a yet smaller contribution. The core's departure from exact isotropy is therefore negligible relative to the ±2° tomographic uncertainty adopted for the State 2 coordinate.

Dynamical uncertainties. The Section 3.3 integration assumes a time-independent ORB tensor during the reorientation, which is valid on timescales shorter than ocean mass redistribution (~day) and solid-Earth bulge re-equilibration (~10^3 yr). A transition completed on 10^3–10^4 yr timescales would be bracketed by these two relaxation scales, introducing a second-order correction to the terminal pole position via the rotational bulge's accommodation to the new axis; the magnitude of this correction is set by the fractional mass redistribution, of order $(C-A)/C \approx 3 \times 10^{-3}$, and is therefore sub-degree.

None of these uncertainties is expected to shift the State 2 coordinate outside the ±2° box reported from tomographic choice; they are acknowledged for completeness. The present paper does not claim that a transition to State 2 is imminent, nor that it will occur within any specific timescale, nor that the reorientation if initiated will complete under any specific dissipation model. What is claimed is that the geographic coordinates of State 2, conditional on a completed reorientation under the coupling regime documented in Paper III and the forcing direction documented in Paper II, are (0.91°S, 3.42°E) with ±2° tomographic uncertainty, and that the angular magnitude of the reorientation is 89.98° ≈ 90° as a geometric invariant of the ORB tensor.

5 CONCLUSIONS

Construction of the Outer Rotating Body inertia tensor from the combined African-plus-Pacific LLSVP mass distribution, using four published tomographic reconstructions at 5×10^5 Monte Carlo samples per province, yields a triaxial tensor whose three principal axes are: I_3 (maximum moment) at (89.19°N, 10.49°E), 0.81° from the present geographic pole (this is State 1); I_2 (intermediate moment) at (0.07°N, 84.69°W) in the Caribbean equator, the unstable saddle axis whose direction from I_3 coincides with Paper II's empirically measured 75°W forcing bearing; and I_1 (minimum moment) perpendicular to both, with its African-hemisphere endpoint at (0.91°S, 3.42°E) in the Gulf of Guinea.

Under the mediated-Dzhanibekov regime implied by the coupling collapse documented in Paper III ($\eta = 0.039$), Euler-equation integration from initial conditions set by Paper II's 75°W bearing confirms that the trajectory from near-I_3 crosses the I_2 saddle and terminates at the African endpoint of I_1. State 2 is therefore located at (0.91°S, 3.42°E) in the Gulf of Guinea, with the new geographic south pole at its antipode (0.91°N, 176.58°W) in the central Pacific Ocean. The angular distance from State 1 to State 2 is $89.98° \approx 90°$, invariant across all four tomographic reconstructions.

The result establishes the post-transition rotational configuration as a derived quantity from the observational record of Papers I–III plus the published LLSVP tomographic consensus, with no free parameter. The reorientation places West and Central Africa at the new geographic north pole, the central Pacific Ocean at the new geographic south pole, and relocates the present continental configuration to distinctly different latitudes and climatic zones than the current frame. Whether and when the reorientation is completed is the subject of Paper VI of this series, which addresses the trigger mechanism and timeline.

DATA AVAILABILITY

IERS EOP 20 C04 pole coordinates are available from https://hpiers.obspm.fr/iers/eop/eopc04/. Seismic tomography models S40RTS (Ritsema et al. 2011) and SEMUCB-WM1 (French & Romanowicz 2015) are available from the IRIS Data Management Center. GEOSYNC Monitor operational pole migration visualisations are available at https://geosyncmonitor.com. The Euler-integration output files cited in Section 3.3 are provided in the supplementary materials accompanying this manuscript. Analysis code developed for the tensor construction and Euler integration in this work is available upon request to the corresponding author.

REFERENCES

Bizouard C., Lambert S., Gattano C., Becker O., Richard J.-Y., 2020. The IERS EOP 14 C04 solution for Earth orientation parameters consistent with ITRF 2014. J. Geod., 93, 621–633.

Cottaar S., Lekić V., 2016. Morphology of seismically slow lower-mantle structures. Geophys. J. Int., 207, 1122–1136.

Dziewonski A.M., Anderson D.L., 1981. Preliminary reference Earth model. Phys. Earth planet. Int., 25, 297–356.

French S.W., Romanowicz B., 2015. Broad plumes rooted at the base of the Earth's mantle beneath major hotspots. Nature, 525, 95–99.

Goldreich P., Toomre A., 1969. Some remarks on polar wandering. J. geophys. Res., 74, 2555–2567.

Gross R.S., 2015. Earth rotation variations — long period. In: Treatise on Geophysics (ed. G. Schubert), 2nd edition, vol. 3, 215–261. Elsevier.

Kirschvink J.L., Ripperdan R.L., Evans D.A., 1997. Evidence for a large-scale reorganization of Early Cambrian continental masses by inertial interchange true polar wander. Science, 277, 541–545.

Koelemeijer P., Deuss A., Ritsema J., 2017. Density structure of Earth's lowermost mantle from Stoneley mode splitting observations. Nat. Commun., 8, 15241.

McNamara A.K., Zhong S., 2005. Thermochemical structures beneath Africa and the Pacific Ocean. Nature, 437, 1136–1139.

Ricard Y., Spada G., Sabadini R., 1993. Polar wandering of a dynamic Earth. Geophys. J. Int., 113, 284–298.

Ritsema J., Deuss A., van Heijst H.J., Woodhouse J.H., 2011. S40RTS: a degree-40 shear-velocity model for the mantle from new Rayleigh wave dispersion, teleseismic traveltime and normal-mode splitting function measurements. Geophys. J. Int., 184, 1223–1236.

Spada G., Ricard Y., Sabadini R., 1992. Excitation of true polar wander by subduction. Nature, 360, 452–454.

Steinberger B., Torsvik T.H., 2010. Toward an explanation for the present and past locations of the poles. Geochem. Geophys. Geosyst., 11, Q06W06.

Torsvik T.H., Steinberger B., Gurnis M., Gaina C., 2012. Plate tectonics and net lithosphere rotation over the past 150 My. Earth planet. Sci. Lett., 291, 106–112.

Torsvik T.H., van der Voo R., Doubrovine P.V., Burke K., Steinberger B., Ashwal L.D., Trønnes R.G., Webb S.J., Bull A.L., 2014. Deep mantle structure as a reference frame for movements in and on the Earth. Proc. Natl. Acad. Sci. USA, 111, 8735–8740.

Tsai V.C., Stevenson D.J., 2007. Theoretical constraints on true polar wander. J. geophys. Res., 112, B05415.

Vaes B., van Hinsbergen D.J.J., Boschman L.M., 2025. Slow true polar wander around varying equatorial axes since 320 Ma. AGU Advances, 6, e2024AV001515.

Yuan Q., Li M., 2022. Instability of the African large low-shear-wave-velocity province due to its low intrinsic density. Nature Geoscience, 15, 334–339.

Zacharias, 2026a. Unprecedented extinction of Earth's Chandler and annual wobbles: evidence for degraded core–mantle boundary coupling, 1846–2026. Manuscript in preparation (Paper I of this series).

Zacharias, 2026b. Systematic directional forcing of Earth's rotation pole toward 75°W: convergent evidence from polar motion cusps, satellite gravimetry and geomagnetic field correlation, 1973–2026. Manuscript in preparation (Paper II of this series).

Zacharias, 2026c. Critical degradation of Earth's rotational coupling revealed by transfer function inversion and broadband polar motion analysis, 1973–2026. Manuscript in preparation (Paper III of this series).

Zacharias, 2026d. Earth's rotational multi-stability: directional evidence for a second principal-axis equilibrium from LLSVP inertia structure, coupling collapse, and contemporary polar motion trajectory, 1962–2026. Manuscript in preparation (Paper IV of this series).